

University of Groningen

## Microstructure and Phase Formation in a Rapidly Solidified Laser-Deposited Ni-Cr-B-Si-C Hardfacing Alloy

Hemmati, Ismail; Ocelik, Vaclav; Csach, Kornel; de Hosson, Jeff Th M.

*Published in:*  
Metallurgical and Materials Transactions A

*DOI:*  
[10.1007/s11661-013-2004-4](https://doi.org/10.1007/s11661-013-2004-4)

**IMPORTANT NOTE:** You are advised to consult the publisher's version (publisher's PDF) if you wish to cite from it. Please check the document version below.

*Document Version*  
Publisher's PDF, also known as Version of record

*Publication date:*  
2014

[Link to publication in University of Groningen/UMCG research database](#)

*Citation for published version (APA):*

Hemmati, I., Ocelik, V., Csach, K., & de Hosson, J. T. M. (2014). Microstructure and Phase Formation in a Rapidly Solidified Laser-Deposited Ni-Cr-B-Si-C Hardfacing Alloy. *Metallurgical and Materials Transactions A*, 45A(2), 878-892. <https://doi.org/10.1007/s11661-013-2004-4>

### Copyright

Other than for strictly personal use, it is not permitted to download or to forward/distribute the text or part of it without the consent of the author(s) and/or copyright holder(s), unless the work is under an open content license (like Creative Commons).

### Take-down policy

If you believe that this document breaches copyright please contact us providing details, and we will remove access to the work immediately and investigate your claim.

*Downloaded from the University of Groningen/UMCG research database (Pure): <http://www.rug.nl/research/portal>. For technical reasons the number of authors shown on this cover page is limited to 10 maximum.*

# Microstructure and Phase Formation in a Rapidly Solidified Laser-Deposited Ni-Cr-B-Si-C Hardfacing Alloy

ISMAIL HEMMATI, VÁCLAV OCELÍK, KORNEL CSACH,  
and JEFF TH.M. DE HOSSON

In this study, microstructural evolutions and phase selection phenomena during laser deposition of a hardfacing Ni-Cr-B-Si-C alloy at different processing conditions are experimentally investigated. The results show that even minor variations in the thermal conditions during solidification can modify the type and morphology of the phases. Higher undercoolings obtained at faster cooling rates suppressed the primary borides and encouraged floret-shape mixtures of Ni and  $\text{Cr}_5\text{B}_3$  via a metastable reaction. Variations in the boride phases are discussed in terms of nucleation- and growth-controlled phase selection mechanisms. These selection processes also influenced the nature and proportion of the Ni-B-Si eutectics by changing the amount of the boron available for the final eutectic reactions. The results of this work emphasize the importance of controlling the cooling rate during deposition of these industrially important alloys using laser beam or other rapid solidification techniques.

DOI: 10.1007/s11661-013-2004-4

© The Minerals, Metals & Materials Society and ASM International 2013

## I. INTRODUCTION

Ni-BASE self-fluxing alloys containing Cr, B, Si, and C are among the most widely used hardfacing alloys for wear and corrosion protection.<sup>[1–4]</sup> Hardness and toughness of these alloys depend on the content of Cr, B, Si, and C. The high-alloy grades of the family contain high quantities of Cr (more than 10 wt pct) and a low ratio of Si to B ( $\text{Si/B} < 3$ ).<sup>[5]</sup> These alloys have been traditionally deposited using various thermal spray techniques. However, laser deposition technologies have also been used in recent years to produce dense Ni-Cr-B-Si-C coatings with metallurgical bonding to the substrate and superior functional properties.<sup>[2,3,6]</sup>

The microstructure of the high-alloy grades of Ni-Cr-B-Si-C laser-deposited coatings consists of a complex mixture of several boride and carbide precipitates along with Ni solid solution dendrites and various binary and ternary Ni-B-Si eutectics.<sup>[7]</sup> Our previous work showed that the high-alloy grades of the Ni-Cr-B-Si-C family have the tendency to develop multiple microstructures from approximately constant alloy chemistry.<sup>[6]</sup> Detailed phase identification confirmed that the microstructural changes were not only morphological variations but also changes in the type of the constituent phases.<sup>[7]</sup> In fact, this explains the diversity of the reports in the literature on the microstructure and phase

constitution of laser-clad Ni-Cr-B-Si-C alloys with comparable chemistries.<sup>[4,8–11]</sup>

The variation in the type and morphology of the constituent phases can be due to changes in chemistry of the alloy or the thermal conditions during solidification. In laser deposition of a fixed alloy composition (*e.g.*, a prealloyed metal powder or wire), compositional changes are mainly caused by various levels of dilution from the substrate.<sup>[12]</sup> For the deposition on carbon steel substrates, various levels of dilution is equivalent to different percentages of iron in the meltpool. Effects of dilution from the steel substrate on the microstructure and phase formation of the alloy of this study were previously studied by us and published elsewhere.<sup>[12]</sup> While the effects of dilution on this alloy system are pronounced mainly at dilutions of more than around 20 pct, even minor variations of thermal conditions during the deposition process may significantly change the properties of Ni-Cr-B-Si-C alloys as will be discussed later.

The focus of the current work is on studying the effects of various thermal conditions on the microstructure and phase formation during solidification of Ni-Cr-B-Si-C alloys. Microstructural evolutions in Ni-Cr-B-Si-C samples deposited using various processing conditions (substrate temperature and deposition speed) are investigated experimentally. The possible mechanisms of microstructural evolutions as well as implications for functional properties are discussed. The current work does not include extensive data on phase identification. Full details on phase identification using various techniques including X-ray diffraction, transmission electron microscopy (TEM) and combination of energy dispersive spectroscopy (EDS), and electron backscatter diffraction (EBSD) were previously published by the authors.<sup>[7]</sup> References will be made when appropriate.

ISMAIL HEMMATI, Ph.D. Student, VÁCLAV OCELÍK, Research Fellow, and JEFF TH. M. DE HOSSON, Professor, Head of Materials Science Group, are with the Department of Applied Physics, Materials innovation institute (M2i), University of Groningen, Nijenborgh 4, 9474 AG Groningen, The Netherlands. Contact e-mail: v.ocelik@rug.nl KORNEL CSACH, Head of Department, is with the Institute of Experimental Physics, Slovak Academy of Sciences, Watsonova 47, 040 01 Kosice, Slovakia.

Manuscript submitted January 24, 2013.

Article published online September 25, 2013

## II. EXPERIMENTAL PROCEDURE

Colmonoy 69 gas-atomized powder from Wall Colmonoy Ltd. was selected as the coating material. This powder has some of the highest alloy contents in Ni-Cr-B-Si-C family. Its high content of Cr and B provides the possibility of having a wide range of phases upon solidification. The coating material was deposited on S355 carbon steel rods with 50 mm diameter using a continuous wave IPG fiber laser with a wavelength of 1.07  $\mu\text{m}$ . Chemical compositions of the coating and substrate materials are presented in Table I. A defocused laser beam was applied with a laser spot size of around 3.5 mm on the substrate surface. Powder feeding system consisted of Metco Twin 10C powder feeder, argon as carrier and shielding gas and a side cladding nozzle with the cyclone and 2 mm nozzle opening. Single layer coatings with a thickness of 0.9 to 1.1 mm each consisting of 5 tracks with 33 pct overlapping were deposited at scanning speeds of 5, 10, and 20 mm/s with laser powers of 800 to 1600 W. At each cladding speed, the powder feeding rate was adjusted to obtain roughly the same thickness of the coating. Dilution from the substrate calculated by dividing the surface area of the deposited layer to the total area of the deposited layer plus remelted substrate<sup>[13]</sup> evaluated from optical microscopy (OM) images was kept in the range of 5 to 15 pct by adjusting the laser power. Samples with the same level of dilution were selected for further microstructural analysis. Hence, for the discussions of this paper, it is possible to assume that all of the samples have approximately the same chemical composition and the microstructural and phase variations were caused by different thermal conditions during solidification. To avoid cracking in the clad layers, the substrate was preheated to 773 K (500 °C) immediately before cladding using an electric furnace. The coated bars were left in the furnace to cool slowly down to the room temperature after cladding.

Samples for scanning electron microscopy (SEM) analyses and hardness measurements were cut from the transversal and longitudinal cross sections and prepared by standard mechanical grinding with suspensions containing 9 and 3  $\mu\text{m}$  diamond particles and polishing with colloidal  $\text{Al}_2\text{O}_3$ . A Philips XL30 field emission gun SEM was used for microstructural observations. Some of the samples were etched with a solution consisting of 7 mL HF, 3 mL  $\text{HNO}_3$ , and 5 mL  $\text{H}_2\text{O}$  in order to reveal the eutectic structures. The eutectic phases were also nicely visible in the as-polished samples under OM.

The multi-track samples exhibited multiple microstructural changes. Identification of the constituent phases proved that these variations included changes in the morphology as well as in phases.<sup>[7]</sup> The complex-

ity of the thermal conditions in multi-track samples made it necessary to start with either simpler cases or cases in which the thermal conditions were better known. In order to establish the relationship between thermal conditions and microstructural evolution, the microstructure and phase constitution of the following four sets of samples were analyzed:

1. *The DTA samples cooled at two different rates of 10 and 100 K/min* The cooling rate of DTA samples is orders of magnitude lower than the cooling rates experienced during laser cladding process (higher than  $10^3 \text{ K/s}$ <sup>[14,15]</sup>). However, the DTA samples are cooled with precisely controlled rates without any dilution effects and can be used to observe the trends in the microstructural changes with increasing the cooling rate.
2. *The single track samples deposited on preheated substrates* In practice, laser cladding of most Ni-Cr-B-Si-C alloys is done on preheated substrates to prevent cracking.<sup>[16]</sup> The single track samples deposited on a preheated substrate at the same cladding speeds are fairly good representatives for the real coatings. Moreover, the absence of overlapping and the shorter deposition time, make these samples easier to analyze.
3. *The single track samples deposited on cold substrates* These samples were meant to simulate the effect of higher cooling rates as the cooling rate for deposition on the cold substrate is higher than the same value for deposition on preheated substrates.<sup>[14]</sup>
4. *The starting powder particles rapidly solidified during the gas atomization process:* The gas-atomized powder particles with a size of 50 to 150  $\mu\text{m}$  can be considered as small droplets of melt which were rapidly solidified with a cooling rate comparable to the cooling rate during laser cladding ( $10^3$  to  $10^5 \text{ K/s}$  for inert gas atomization<sup>[17]</sup>). The powder particles also contain no dilution effects. The small liquid droplets may contain variable amounts of impurities and heterogeneous nucleation sites. Hence, they can solidify at different levels of undercooling.<sup>[18]</sup>

Our previous study<sup>[12]</sup> showed that columnar dendrites of Ni which always formed in the deposits adjacent to the deposit-substrate interface were closely related to the iron-rich layer next to the interface. This layer had a lower hardness and probably a reduced corrosion resistance. In order to study the grain structure in the vicinity of the deposit-substrate interface and the transition of columnar dendrites to equiaxed dendrites, EBSD scans were performed at an acceleration voltage of 30 kV. Evidence of peritectic transformation of one type of boride to another type was frequently observed in the deposits. To evaluate the phases involved in the transformation, a combination of EDS and EBSD were used for phase identification. EBSD was also employed to study the crystal orientation of the competing phases. Full details on EBSD sample preparation and data cleaning procedure as well as the EDS/EBSD combination for phase identification are presented elsewhere.<sup>[7]</sup> Hardness of different microstructures

**Table I. Nominal Chemical Composition of Substrate and Clad Materials (Weight Percentage)**

Material	Ni	Fe	Cr	Si	C	B	Mn	Mo	Cu
Colmonoy 69	bal.	3	16.5	4.8	0.55	3.6	—	3.5	2.1
S355	0.7	bal.	0.2	0.55	0.12	—	1.65	0.08	0.3



was measured by a CSM Revetest machine using Vickers indenter at a load of 4.9 N.

### III. RESULTS

#### A. Microstructural Changes in Multi-Track Samples

Figure 1(a) presents the OM image from transversal cross section of a five-track deposit (first track on the left

side). The labels in Figure 1(a) denote locations in different tracks from which the dominant microstructures are presented by the SEM images of Figures 1(b) through (g). Most of the SEM observations were performed using backscattered electron (BSE) detector on as-polished samples. BSE imaging proved to be a very useful tool in microstructural study of these deposits because of its ability to generate contrast based on the atomic number. This made it easy to visualize

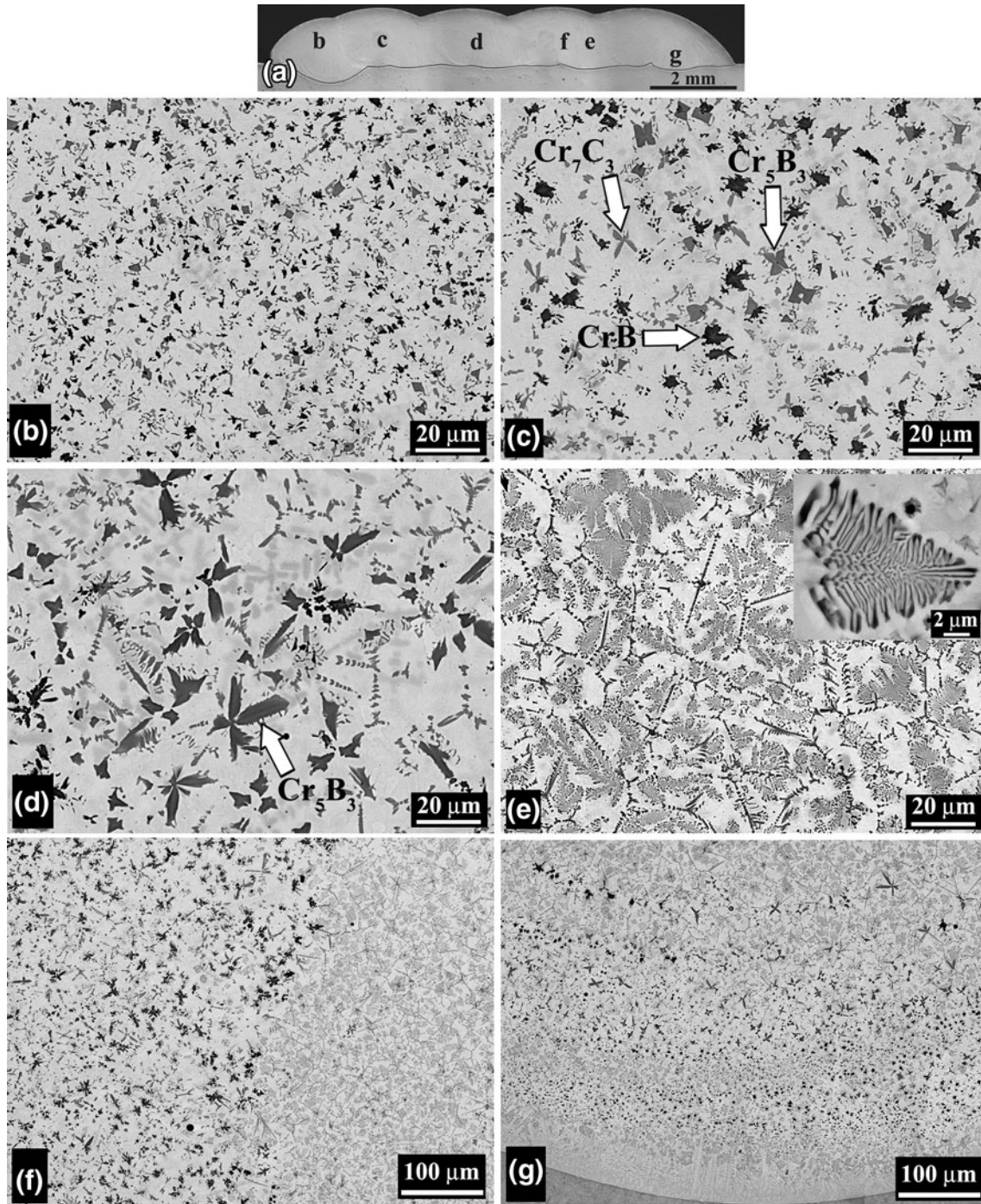


Fig. 1—(a) OM image showing the transversal cross section of a five-track deposit. (b) through (e) SEM–BSE images showing the microstructure of different tracks as labeled in (a). (f) and (g) SEM–BSE images showing the abrupt or gradual microstructural changes in the locations labeled in (a) as (f) and (g).

boride and carbide precipitates on the as-polished samples. Substantial differences in size, shape, and composition of the precipitates could be observed from the first track to the last one as shown in Figures 1(b) through (e). Dilution in the second to fifth tracks was less than dilution for the first track as a result of overlapping with the existing deposit.

In tracks 1 and 2, the precipitates were mostly blocky CrB (Figures 1(b) and (c)). The main difference between these two tracks was the bigger sizes of precipitates in track 2. Such a difference is an outcome of the higher dilution in the first track which diminishes the boride precipitates.<sup>[12]</sup> In track 3, the butterfly-shape  $\text{Cr}_5\text{B}_3$  precipitates were the dominant borides along with some CrB and a number of dendritic  $\text{Cr}_7\text{C}_3$  (Figure 1(d)). In tracks 4 and 5, the microstructure changes entirely and consists of a mixture of floret-shape structures and dendritic  $\text{Cr}_7\text{C}_3$  (Figure 1(e)). The inset in Figure 1(e) shows a close-up view of what is called the “floret-shape structure” throughout this text. This structure is the product of a metastable eutectic reaction at around 1373 K (1100 °C) and consists of  $\text{Cr}_5\text{B}_3$  and Ni layers<sup>[7]</sup> (in Figure 1(e), dark and bright layers, respectively). In some cases, abrupt microstructural changes were found inside one track or from one track to the subsequent one as shown in Figure 1(f). The abrupt changes indicate sharp thresholds in the system at which variations in phase formation could occur. Sometimes these microstructural variations could happen in one track from bottom to top of the track. Figure 1(g) shows the cross section of track 5 (position g) in which after a thin layer of columnar dendrites adjacent to the substrate-clad interface, first CrB and then  $\text{Cr}_5\text{B}_3$  were formed and finally a mixture of floret-shape structures and dendritic  $\text{Cr}_7\text{C}_3$  became dominant and covered most of the deposit. The precipitate-free layer of columnar dendrites was present in all of the deposited samples. Thickness of this layer depends on the level of dilution.<sup>[12]</sup>

Each of the microstructures shown in Figures 1(b) through (e) has a different hardness with (b) showing the lowest hardness of around 500 HV and (e) the highest of around 900 HV. More details on hardness changes can be found elsewhere.<sup>[6]</sup>

The multitude of microstructural variations and phase changes in the multi-track deposits proved that an experimental analysis of the microstructural evolutions directly on multi-track samples is not easy to do. As explained before, the variation in the type and morphology of the constituent phases can be attributed to changes in chemistry of the alloy or the thermal conditions during the solidification. The OM image of Figure 1(a) shows that after the first track, the dilution level is almost the same. So, it is reasonable to assume that variations in the thermal conditions were responsible for the observed microstructural changes.

The Ni-Cr-B-Si-C coatings are very susceptible to cracking.<sup>[19]</sup> Reducing the cooling rate after deposition using preheating and postheating is a widely used method to lower the cracking tendency of these materials.<sup>[16]</sup> During the deposition of the multi-track samples on preheated substrates and before reaching a quasi-steady state, on one hand the heat accumulation

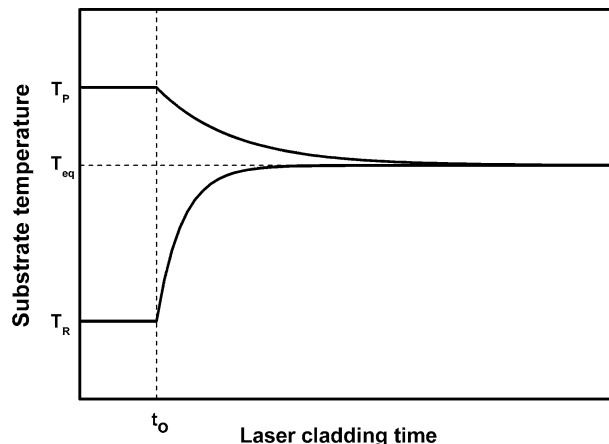


Fig. 2—Dependence of the substrate temperature near cladding zone before reaching equilibrium temperature ( $T_{eq}$ ) as a function of time for deposition on substrates at room temperature ( $T_R$ ) or preheated to  $T_P$ .

as a result of the laser beam energy will reduce the cooling rate and on the other hand, cooling of the substrate from preheating temperature will increase it. Such a situation is different from deposition on a cold substrate in which cooling rate gradually and continuously decreases as a result of heat accumulation in the substrate. The temperature variations of the cold and preheated substrates during deposition process are schematically represented in Figure 2.

## B. Microstructural Evolutions in DTA Samples

The DTA thermograms were analyzed for their thermal events and microstructure of the relevant DTA samples was observed by SEM. Figure 3 shows the DTA graphs and the microstructure of the solidified samples. Contrary to graph (b) which contains only three thermal events below 1473 K (1200 °C), the graph of (a) has several peaks in the temperature range of 1773 K to 1473 K (1500 °C to 1200 °C) as well as the same peaks in (b). The diversity of the phases in the microstructure of Figure 3(c) confirms that solidification of the intended composition at a slower rate generated multiple borides with different morphologies. On the other hand, increasing the cooling rate suppressed the blocky borides and most of the microstructure consisted of floret-shape structures in a matrix of Ni along with Ni-B-Si eutectics.

## C. Microstructural Evolutions in Single Track Samples

Figure 4 shows the microstructure of single tracks deposited on preheated bars at deposition speeds of 5, 10, and 20 mm/s. After deposition at the speed of 5 mm/s, the microstructure consisted of blocky borides (mainly CrB) as visible in the inset of Figure 4(a). As shown in Figure 1(f), abrupt microstructural changes could occur in this alloy. The same phenomenon happened from bottom to top of the single track deposited at 10 mm/s. Figure 4(c) shows a close-up view of this transition in which the blocky borides are abruptly substituted with



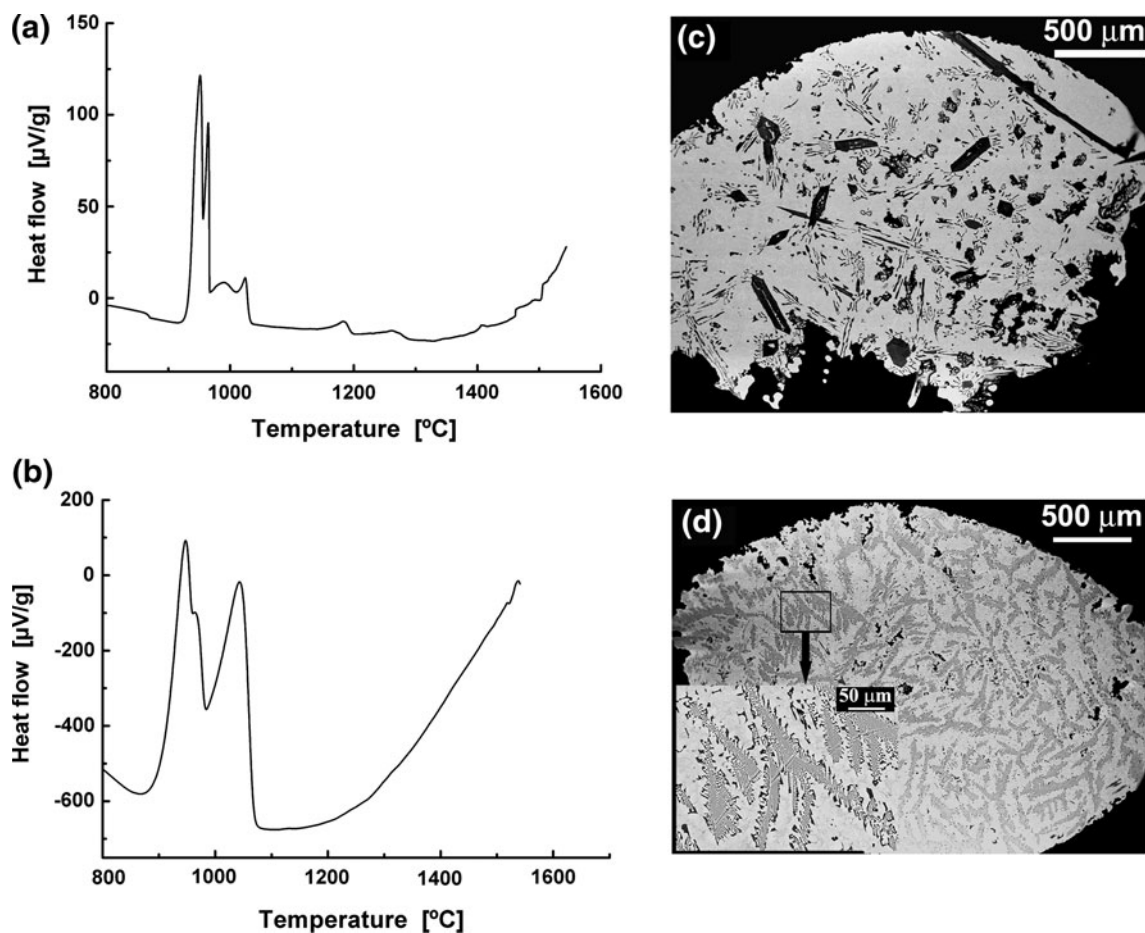


Fig. 3—DTA graphs showing the thermal response of the alloy cooled at (a) 10 K/min and (b) 100 K/min. SEM microstructural images of the samples cooled at 10 and 100 K/min are shown in (c) and (d), respectively.

floret-shape structures at the upper half of the track. Microstructure of the track deposited at 20 mm/s contained very few blocky borides and majority of the microstructure consisted of floret-shape structures along with dendritic  $\text{Cr}_7\text{C}_3$  as shown in the inset of Figure 4(d).

The single track samples deposited on the cold bars at 5, 10, and 20 mm/s contained negligible amount of blocky borides. Figure 5 shows the SEM–BSE image from the microstructure of the single track deposited at the lowest cladding speed of this study (5 mm/s). The insets show that after a precipitate-free layer of columnar dendrites close to the interface, the microstructure contains only floret-shape structures plus numerous dendritic  $\text{Cr}_7\text{C}_3$ .

#### D. Microstructure of the Powder Particles

Figure 6(a) shows the SEM micrograph of the gas-atomized powders. The diameter of the powder particles was in the range of 50 to 150  $\mu\text{m}$ . Figures 6(b) through (d) show the microstructure of various powder particles as observed by SEM–BSE. Although the powder particles were from the same batch and their diameters were comparable, their microstructures were very different. In the powder particle of Figure 6(b), CrB is the main

boride precipitate along with some butterfly-shape  $\text{Cr}_5\text{B}_3$  and flower-shape  $\text{Cr}_7\text{C}_3$  as indicated by arrows. On the other hand, the powder particle of Figure 6(c) shows a mixture of several phases including large quantities of  $\text{Cr}_5\text{B}_3$  as well as floret-shape structures and some CrB. The powder particle of Figure 6(d) has a microstructure consisting of the same phases as in (b) and (c) but in much larger numbers and significantly smaller sizes which shows that this particle experienced a significant amount of undercooling. The microstructural images of Figures 6(b) through (d) show that even with the same chemistry and diameter, the melt droplets of the intended composition can develop significantly different phases and microstructures. The morphology of the constituent phases in the powder particles are very similar to that of the same phases formed during laser deposition.

#### E. Observation of the Eutectic Structures

Although BSE imaging was a very effective method to observe boride and carbide precipitates, fine Ni–B–Si eutectics with 100 nm thick layers<sup>[7]</sup> and Ni solid solution dendrites could not be properly distinguished in the BSE images. OM was capable of generally showing the eutectic areas and Ni grains. But it was

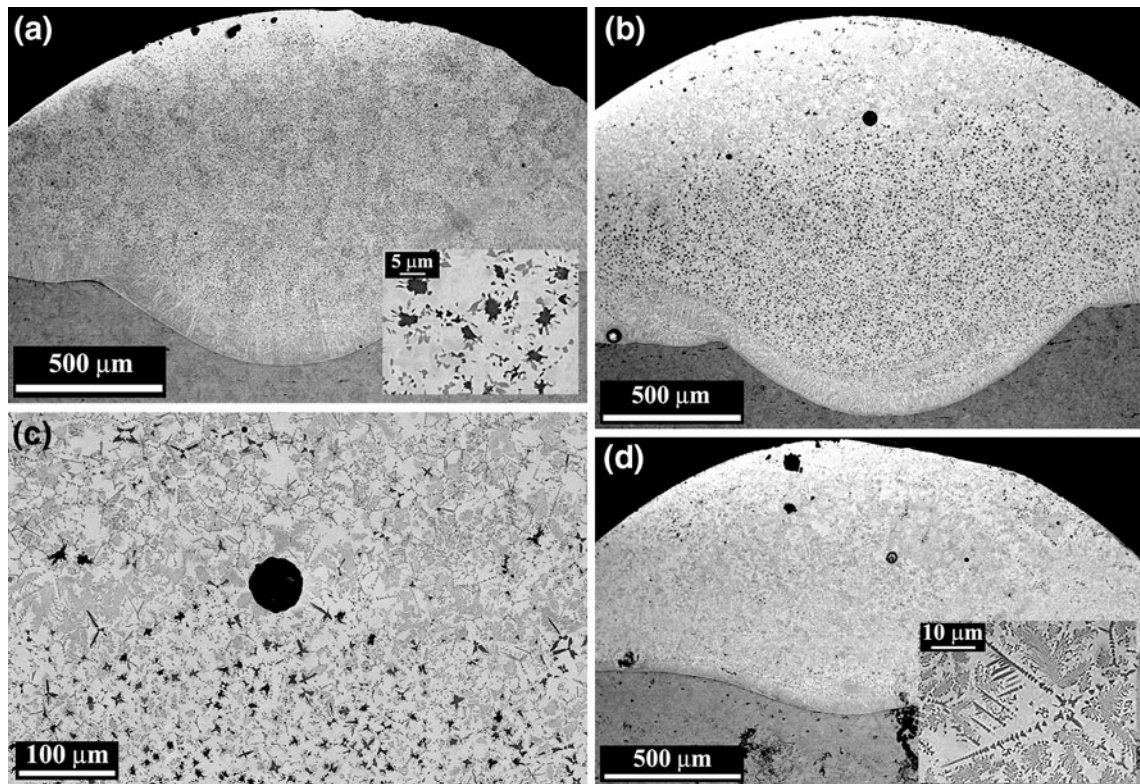


Fig. 4—Microstructure of single track samples deposited on preheated substrate at different cladding speeds (a) 5 mm/s, (b) 10 mm/s, (c) close-up of the microstructural transition at the top of sample (b), (d) 20 mm/s.

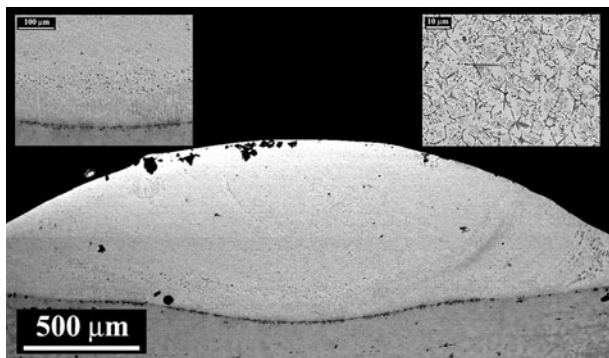


Fig. 5—Cross section of the single track deposited on cold substrate at 5 mm/s. Insets show microstructures close to deposit-substrate interface (left) and the rest of the deposit (right).

necessary to etch the samples and perform SEM observation to reveal the details of the eutectic structure. Figure 7(a) shows an example of the etched microstructures in which the eutectic layers are clearly visible in the Secondary Electron (SE) SEM image. Dendrites of Ni solid solution could be observed as well. These two structures are the ones which appear as a bright background in the BSE images of the earlier figures. Previous TEM phase identification showed that the eutectic structures in this alloy are combinations of both equilibrium and non-equilibrium binary and ternary Ni-B-Si eutectic phases such as  $\text{Ni}_3\text{B}$ ,  $\text{Ni}_2\text{B}$  and  $\text{Ni}_3\text{Si}$ .<sup>[7]</sup>

Figures 7(b) and (c) present the main microstructures as observed by OM. The microstructure shown in Figure 7(b) is similar to those shown in Figures 1(c) and 4(a) and the one presented in Figure 7(c) is the same as those in Figures 1(e) and 4(d). Although the details of the eutectic structures cannot be resolved as in Figure 7, the OM images provide the possibility of measuring the total area percentage of the eutectics. This percentage was calculated using image analysis to be approximately 20 and 35 for the microstructures in Figures 7(b) and (c), respectively. These numbers show that the microstructures with blocky borides or floret-shape structures are not only different in the type of their boride phases, but also in the amount of the eutectics.

#### F. Hardness Variations

The implications of the microstructural changes for hardness of the deposits were evaluated by measuring microhardness from bottom towards top of the track in Figure 1(g). This track contained three distinctive regions: a precipitate-free layer of columnar Ni dendrites next to the clad-substrate interface, a layer containing blocky borides and finally, majority of the deposit consisting of floret-shape structures and dendritic  $\text{Cr}_7\text{C}_3$ . The hardness graph of Figure 8(a) similarly shows three regions with different hardness ranges: close to the interface with a hardness of around 500 HV, a second region of around 750 HV and a final part with the highest hardness of around 900 HV.



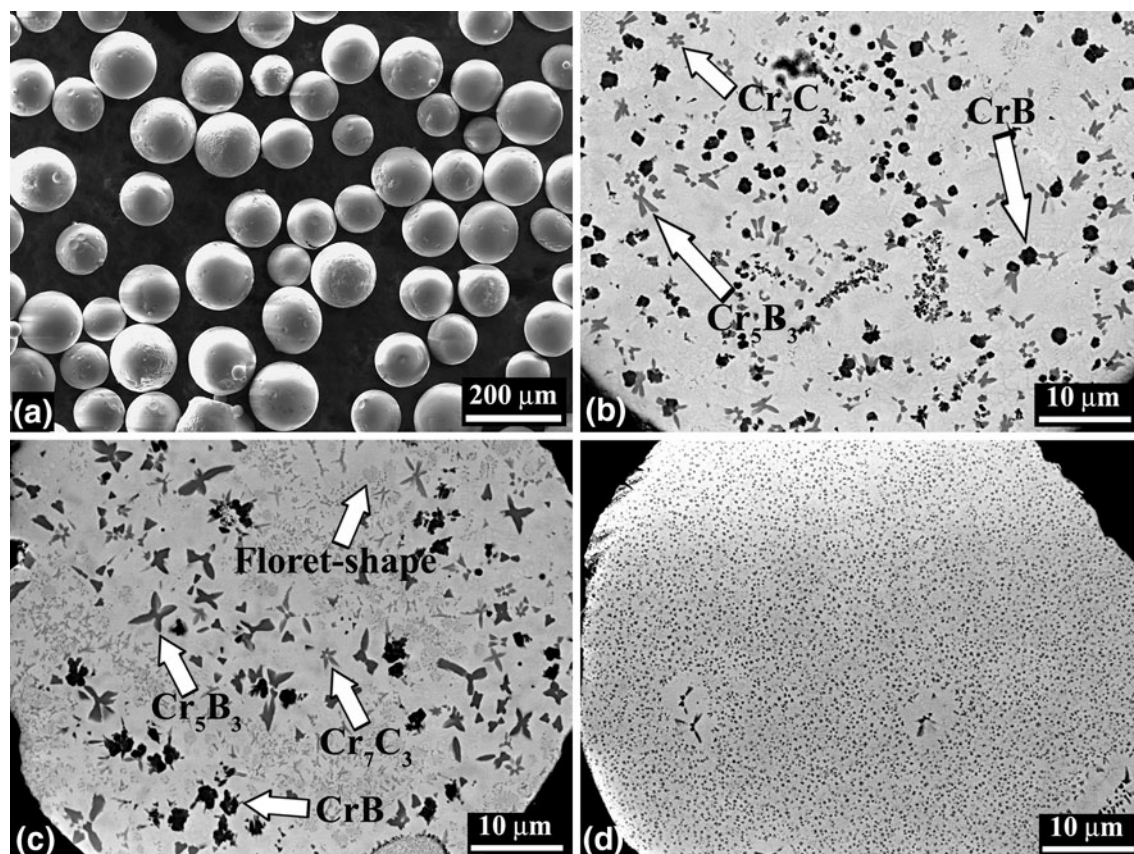


Fig. 6—(a) SEM micrograph of the gas-atomized powder particles, (b) through (d) BSE images showing the cross section of several powder particles with various microstructures.

Observation of the individual hardness indents confirmed that the three hardness ranges in Figure 8(a) correspond to the three microstructural regions in Figure 1(g). The highest hardness belonged to the indents which were positioned entirely on the eutectic structures. The hardness indent of Figure 8(b) shows an example where hardness was 1073 HV. It seems that eutectic structures contribute significantly to the hardness of these alloys. In fact, the highest hardness belongs to the microstructure shown in Figure 7(c) which contains a higher percentage of the eutectic phases.

### G. Other Microstructural Phenomena

In addition to the microstructural variations mentioned before, the three following phenomena were frequently observed. These phenomena provide clues about the variations of thermal conditions during solidification or the sequence of phase formation reactions as will be discussed later.

#### 1. Columnar to Equiaxed Transition in Ni Dendrites

The morphological transition in Ni solid solution dendrites from columnar to equiaxed as shown in Figures 9(a) and (b) was a common feature in all of the samples. This columnar to equiaxed transition (CET) could be seen at the bottom of the deposits and close to deposit–substrate interface. A very thin layer of

planar growth was present at all interfaces with an extension of few micrometers. This planar growth zone became unstable as solidification proceeded and broke down into cellular grains. EBSD was used to study the grain structure and the morphological changes of the Ni grains from bottom to top of the deposits. In order to correctly evaluate the shape of the Ni grains, EBSD scans were performed on the longitudinal cross section at the middle of the track as recommended previously.<sup>[20]</sup> Figure 9(d) shows the EBSD inverse pole figure (IPF) map of the interface region shown in (c). The IPF map is superimposed on the image quality map and the dark areas are filtered because of low indexing quality. Figure 9(d) clearly shows the change in morphology of Ni dendrites from columnar to equiaxed from bottom towards the top of the deposit. The significance of this change is that the columnar structure of Ni grains hinders the flow in the melt pool and prevents compositional homogenization of the melt. It was previously shown that there is a direct relationship between extent of the columnar structure adjacent to the interface and the thickness of the iron-rich layer.<sup>[12]</sup> Higher Fe content of the interfacial region (caused by dilution from the steel substrate) modifies the solidification path of the alloy which reduces the amount of Ni-B-Si eutectics and suppresses the precipitation of the primary boride.<sup>[6,12]</sup> These changes will diminish the hardness of the deposit in the interfacial region as shown in Figure 8(a).



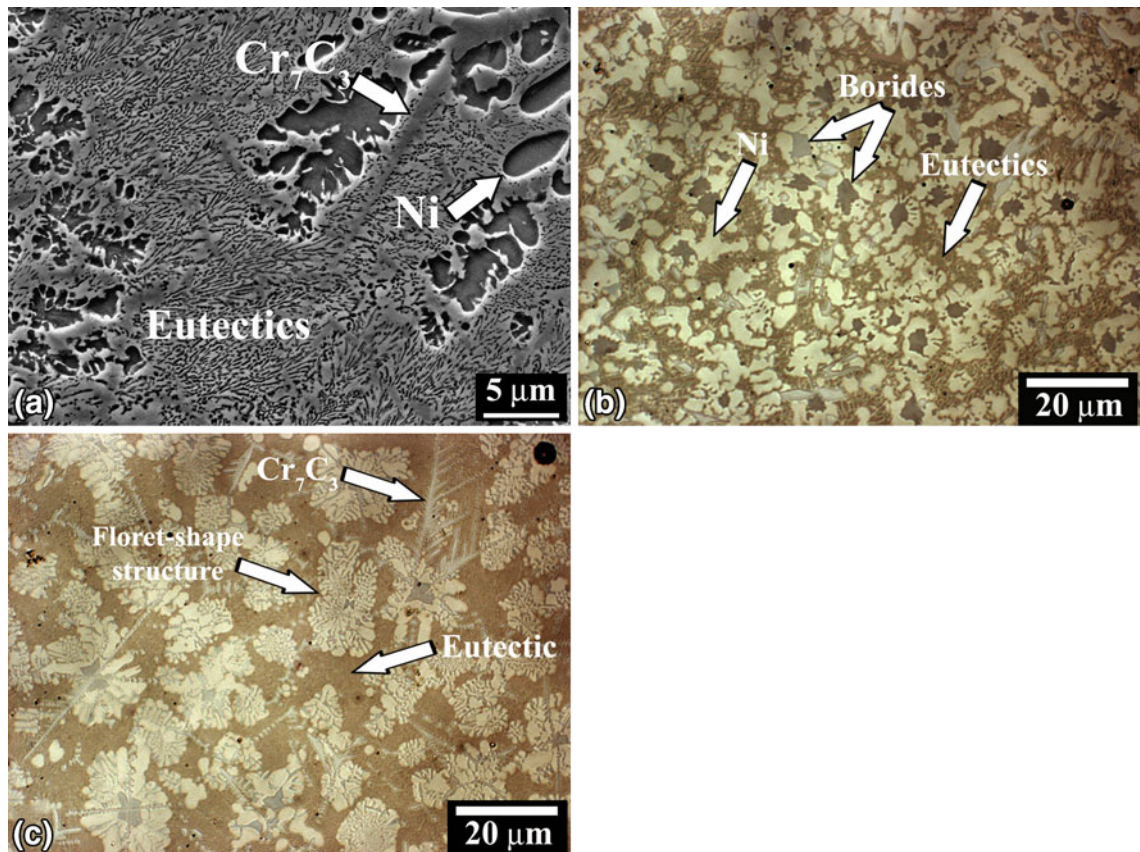


Fig. 7—(a) SEM image showing an example of the eutectic structure after etching. (b) and (c) OM images of two different microstructures as presented in Figs. 1(c) and (e). The difference in the amount of eutectics is noticeable.

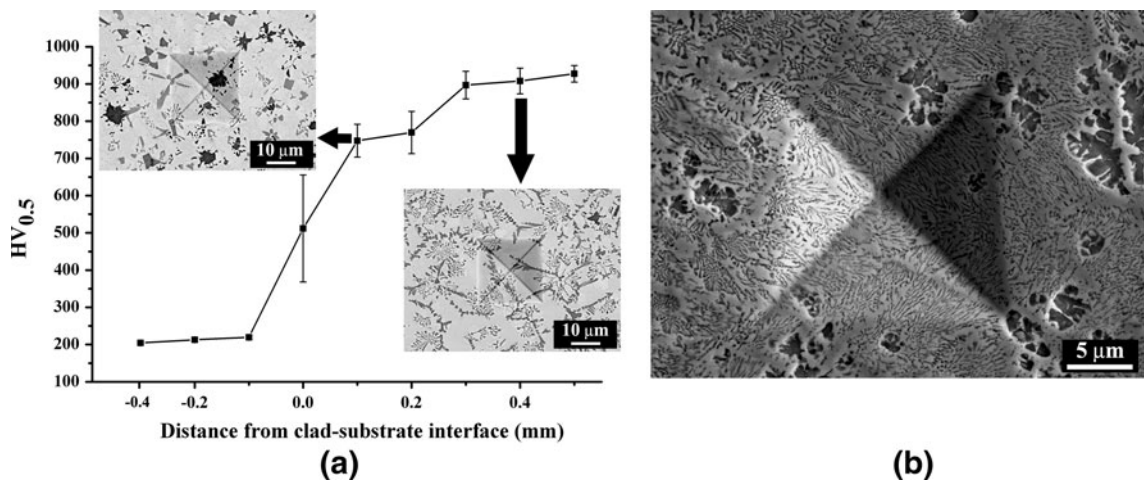


Fig. 8—(a) Variations of microhardness along the depth of the track shown in Fig. 1(g), (b) an indent entirely located on the eutectic structure with a hardness of 1073 HV.

## 2. Peritectic Transformation of CrB

The BSE image of Figure 10(a) shows a microstructure in which several boride precipitates (with the darkest contrast and indicated by arrows) are enveloped in other precipitates. Such a configuration is usually formed during peritectic reactions which the Cr-B system contains a number of them as shown in Figure 10(b). Based on the knowledge obtained so far about the prevalent

types of borides in this system and also based on the contrast of the phases in the BSE image,<sup>[7]</sup> it is possible to predict that the darker borides in Figure 10(a) are CrB and the ones surrounding them are Cr<sub>5</sub>B<sub>3</sub>. In fact, the peritectic reaction of  $L + CrB \rightarrow Cr_5B_3$  can be found in the binary Cr-B phase diagram at around 2173 K (1900 °C).<sup>[21]</sup> EDS/EBSD phase identification was done to conclusively determine the type of the phases involved



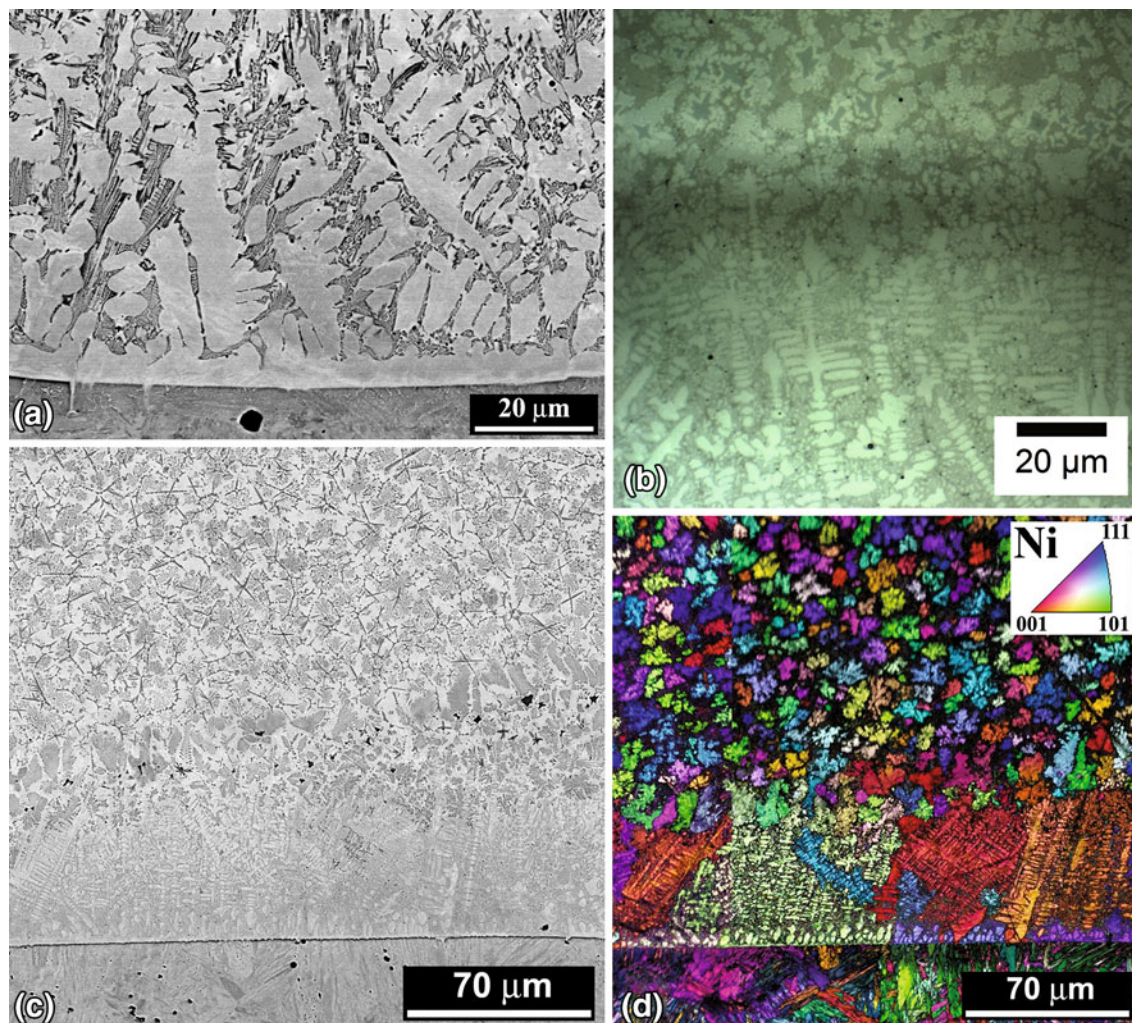


Fig. 9—(a) SEM-BSE image showing the planar layer at the interface and the change to columnar structure, (b) OM image of the CET region, (c) SEM-BSE image of the interface region and (d) IPF + IQ map showing the CET from bottom to the top of the track shown in (c). Boundary misorientation is 5 deg.

in these structures. According to the EBSD phase map of Figure 10(d), the larger precipitate in Figure 10(c) is a single crystal  $\text{Cr}_5\text{B}_3$  (tetragonal structure with lattice parameters of  $a = 0.537$  nm and  $c = 1.0188$  nm) which is formed around a polycrystalline CrB (orthorhombic structure with lattice parameters of  $a = 0.2966$  nm,  $b = 0.7867$  nm, and  $c = 0.2932$  nm). It can be seen in Figure 10(a) that the peritectic transformation, *i.e.*, thickening of the peritectic envelope<sup>[22]</sup> is in different stages for different precipitates. In some cases, the CrB precipitate is almost entirely transformed to  $\text{Cr}_5\text{B}_3$  while in other cases it is not even fully surrounded. This is because of the fact that once CrB is covered with a layer of  $\text{Cr}_5\text{B}_3$ , thickening of the  $\text{Cr}_5\text{B}_3$  layer will be controlled by the diffusion of B, Cr and other elements through the layer. The microstructures represented in Figures 1(d) and 10(a) shows that  $\text{Cr}_5\text{B}_3$  could form directly from the melt as well as through peritectic reaction. This coexistence shows that the peritectic reaction of  $\text{L} + \text{CrB} \rightarrow \text{Cr}_5\text{B}_3$  did not start at the peritectic temperature, most probably because of the need for some level of undercooling.<sup>[23]</sup> At temperatures below the peritectic

reaction, the product of the reaction had the possibility to form directly from the melt. Hence, the  $\text{Cr}_5\text{B}_3$  precipitates have formed either around the existing CrB particles or as independent precipitates.

### 3. Nucleation of Cr Carbides on Borides

$\text{Cr}_7\text{C}_3$  is the dominant type of carbide in this system.<sup>[7]</sup> Two morphologies of  $\text{Cr}_7\text{C}_3$  were found; flower-shape (Figure 6(b)) and dendritic (Figure 11). The first morphology was common in microstructures with blocky borides while the dendritic morphology was prevalent in the microstructure consisting of floret-shape structures (Figure 1(e)). An interesting feature of dendritic  $\text{Cr}_7\text{C}_3$  was its nucleation on CrB or  $\text{Cr}_5\text{B}_3$  precipitates as shown in Figure 11.

## IV. DISCUSSION

### A. Mechanisms of Microstructural Evolution

The observed microstructures in the laser-deposited Colmonoy 69 can be classified into two general



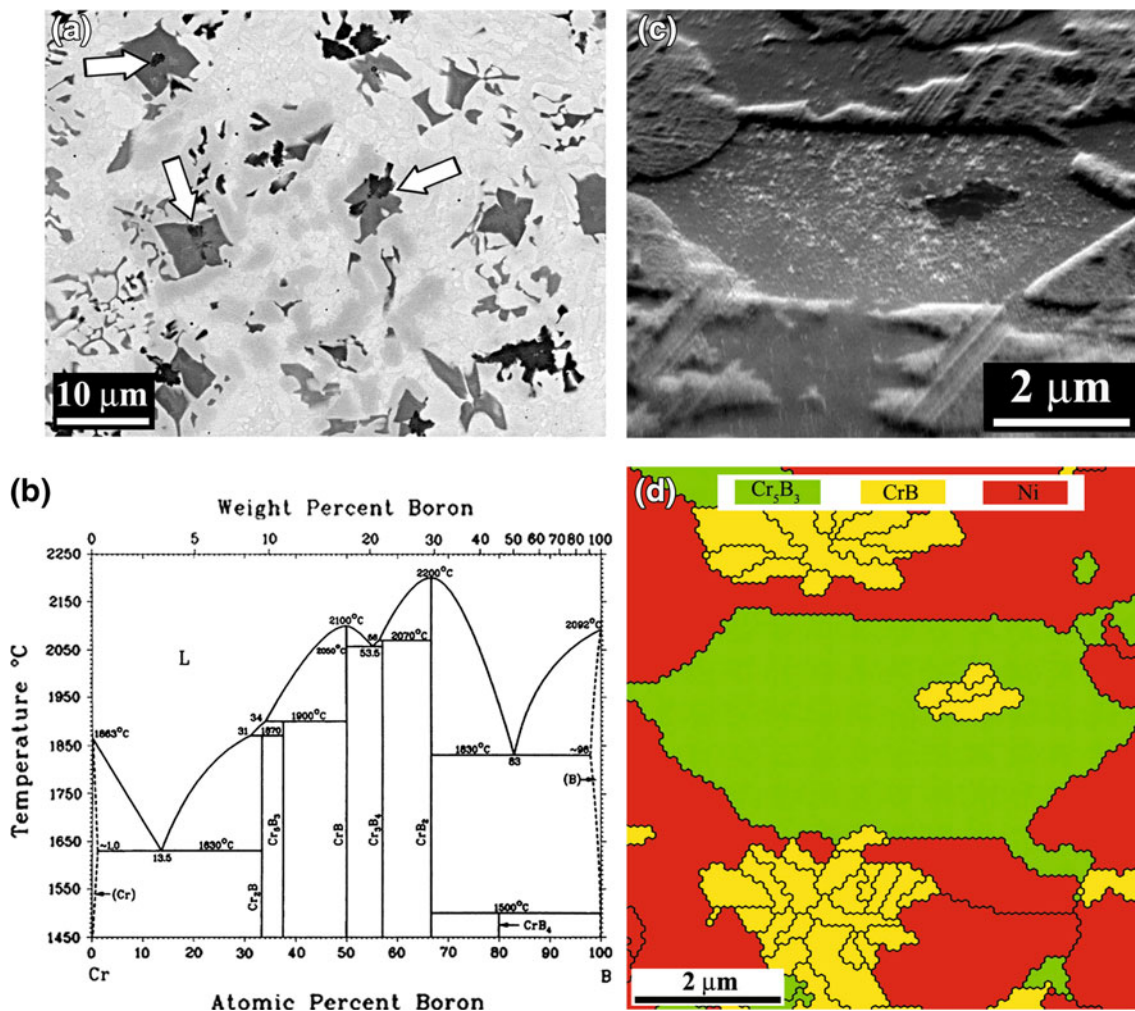


Fig. 10—(a) SEM-BSE image showing multiple cases (highlighted by arrows) of boride precipitates enveloping another phase. Such features were frequently observed in the microstructures with CrB as the main boride phase, *e.g.*, Fig. 1(c). (b) Cr-B phase diagram, (c) SEM image of one boride precipitate which surrounds another phase with a darker contrast, (d) EBSD phase map of the structure in (b) showing a CrB precipitate surrounded by Cr<sub>5</sub>B<sub>3</sub>.

categories: the ones with primary Cr boride/carbides (which could be found in the equilibrium phase diagrams, *e.g.*, CrB and Cr<sub>5</sub>B<sub>3</sub>) along with lower contents of Ni-B-Si eutectics (Figures 1(c), (d) and 7(a)) and the one containing floret-shape structures and higher contents of Ni-B-Si eutectics (Figures 1(e) and 7(b)). As both of these microstructures were also observed in the DTA samples, analysis of the relationship between thermal conditions and the microstructural evolution can be started with the DTA samples in which the solidification conditions are relatively well-known.

The solidification path of this alloy involves precipitation of several borides and carbide as well as Ni solid solution and Ni-B-Si eutectic phases.<sup>[7]</sup> Due to this multiplicity of phases and the absence of an accurate multi-component phase diagram, a precise interpretation of the DTA curves is not easy. The primary phases in this system are Cr borides and carbide. Absence of the thermal events in the DTA curve of the sample cooled at 100 K/min (Figure 3(b)) shows that increasing the cooling rate in this system suppress the primary phase

formation reactions. At higher cooling rates, most of the boron content was consumed to produce floret-shape structures (Figure 3(d)). These structures were previously characterized to be mixtures of Ni and Cr<sub>5</sub>B<sub>3</sub> which form through a metastable eutectic reaction at around 1373 K (1100 °C).<sup>[7]</sup> This temperature roughly corresponds to the onset temperature of the first peak in the DTA graph of Figure 3(b). The DTA peaks at temperatures less than 1273 K (1000 °C) belong to the Ni-B-Si binary and ternary eutectic reactions and do not show substantial differences for the two cooling rates. Hence, the largest impact of the cooling rate on the solidification pathway of this alloy was during formation of the boride phases.

By extending the outcomes from analysis of the DTA samples to the single tracks, similar trends for the effect of cooling rate on phase formation could be observed. Figure 4 shows that transition from the first category of microstructures to the second one could occur inside a single track from bottom to top of the melt pool. At higher deposition rates, such a transition happened

earlier, *i.e.*, closer to the deposit–substrate interface. Consequently, while the single track deposited at 5 mm/s only contained the first category of microstructure (Figure 4(a)), the track deposited at 10 mm/s had a mixed microstructure (Figures 4(b) and (c)) and the one deposited at 20 mm/s entirely consisted of floret-shape structures plus dendritic carbides (Figure 4(d)).

The microstructures of Figures 4(a) and (d) are the ones which formed at the lowest and the highest cladding speeds or substrate preheating temperatures, respectively. Hence, they can be used to establish the microstructure-cooling rate relationships in the studied coatings. The cooling rate at the middle of single tracks deposited on preheated substrates at 5 and 20 mm/s was estimated by a simple laser melting model presented by

Berjeza<sup>[24]</sup> using the parameters presented in Table II. The cooling rates for microstructures presented in Figures 4(a) and (d) were estimated to be around  $3.9 \times 10^3$  and  $6.6 \times 10^4$  K/s, respectively. These values are in the same range as calculated previously by finite element modeling for laser-deposited coatings.<sup>[14,15]</sup>

A closer look at how thermal parameters vary from bottom to the top of the melt pool during solidification of a single track can further clarify the microstructural evolutions. The most important variables in the solidification of the laser-deposited coatings are the solid–liquid interface growth velocity  $V$  (mm/s) and the temperature gradient in the liquid ahead of the solid–liquid interface  $G$  (K/mm). Combination of  $G$  and  $V$  makes two important combined parameters, namely the cooling rate  $\dot{T}$  (K/s) which is equal to  $G \cdot V$  in directional growth and the interface stability criterion (for constitutional undercooling)  $G/V$ . Kurz and Trivedi<sup>[25]</sup> analyzed the variations of the four above-mentioned parameters along the depth of the laser-deposited coatings. Their results showed that  $V$  is zero at the bottom of the melt pool but rapidly increases to values equal to the laser beam transverse speed at the top of the track.  $G$  has an opposite trend with the highest value at the deposit–substrate interface and falling towards the top. This combination results in the highest value of  $G/V$  at the deposit–substrate interface with a continuous decrease towards the top of the melt pool. The cooling rate ( $G \cdot V$ ) follows an opposite trend with the highest value at the top of the melt pool and continuously decreasing towards the deposit–substrate interface. This can be explained by the fact that heat extraction is mainly done by the substrate through the deposit–substrate interface. Hence, the cooling rate is the lowest close to that area because the heat released further away has to pass through the interface region.

The microstructural evolutions in the single track samples showed that increasing the cooling rate either because of the variations in  $G \cdot V$  along the depth of the melt pool or as a result of deposition on cold substrates will suppress the blocky borides and encourage floret-shape structures. Furthermore, the reduction of  $G/V$  from bottom to top of the melt pool is responsible for CET in the Ni dendrites. The  $G/V$  ratio describes the level of interface instability and determines the solidification mode. As this ratio decreases, the planar solid–liquid interface becomes unstable. As a result, the microstructure will change from planar to cellular, then to columnar dendrites and finally to equiaxed dendrites.<sup>[26]</sup> All of these transitions could be found in the analyzed samples as presented in Figure 9.

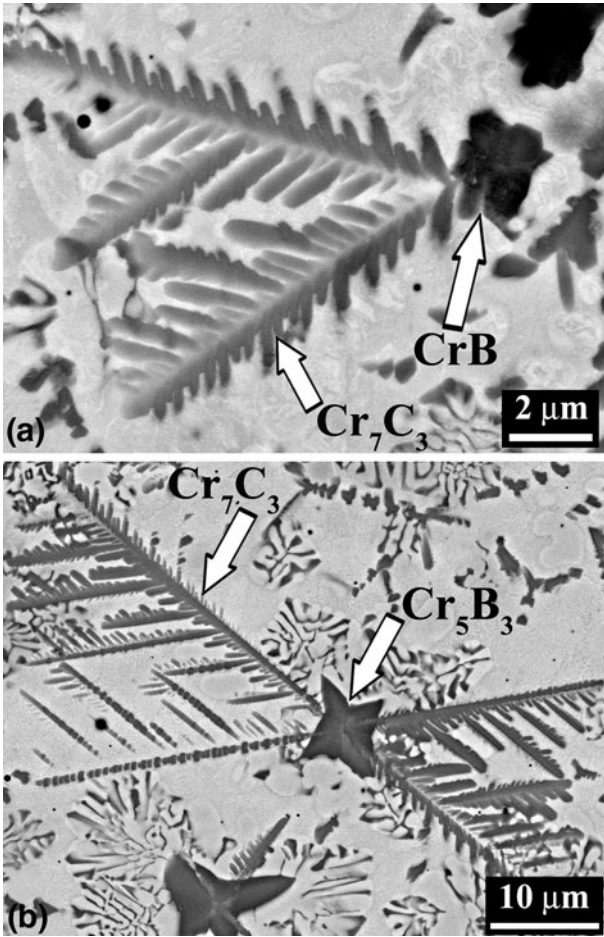


Fig. 11—Nucleation of dendritic Cr<sub>7</sub>C<sub>3</sub> on (a) CrB and (b) Cr<sub>5</sub>B<sub>3</sub>.

**Table II. The Input Parameters to Estimate the Cooling Rates Using the Model Presented by Berjeza<sup>[24]</sup> for Single Track Samples Deposited on Substrate Preheated to 773 K (500 °C)**

Cladding Speed (mm/s)	Laser Power (W)	Beam Spot Size (mm)	Heat Capacity (J/Kg K)	Thermal Conductivity at 1144 K (871 °C) (W/m K)	Density (g/mm <sup>3</sup> )
5	800	3.57	444	28.8	8.06
20	1400	3.57	444	28.8	8.06

The thermal properties are extracted from Ref. [32].



Based on the findings for the relationships between the processing conditions and microstructures for DTA samples and single track deposits, it is possible to interpret the microstructural changes in the multi-track samples. It was found that the microstructure consisting of floret-shape structures and dendritic Cr carbides forms at higher cooling rates. This microstructure also occurred in the fourth and fifth tracks in the multi-track sample deposited at 5 mm/s (Figure 1) and even earlier in samples deposited at 10 and 20 mm/s. It seems reasonable to conclude that the cooling rate has increased as multi-track deposition on preheated bars proceeded. In other words, the effect of substrate cooling was more pronounced than the effect of heat accumulation so that the substrate cooled down below the initial preheating temperature of 773 K (500 °C). The cooling rate required for the microstructural transition was reached earlier at higher deposition speeds because the interface growth velocity ( $V$ ) and hence the cooling rate ( $G \cdot V$ ) are directly proportional to the deposition speed.<sup>[20]</sup>

### B. Phase Selection Phenomena

Contrary to the CET which is a morphological change, transition of the boride precipitates from CrB to Cr<sub>5</sub>B<sub>3</sub> and finally to floret-shape structures (which are mixtures of Cr<sub>5</sub>B<sub>3</sub> and Ni) is a phase change. As the composition of the melt was approximately constant in all experiments, position of the melt in the multi-component phase diagram did not significantly change. On the other hand, the two categories of microstructures did not coexist in the studied samples, *i.e.*, in every condition one category was preferably formed. This means that the transitions in the type of the boride phases as a consequence of variations in the thermal conditions can be regarded as a series of phase selection processes. Formation of all the observed phases consists of nucleation and growth steps. Hence, the phase selection phenomena can be examined in terms of relative nucleation and growth kinetics of the competing phases.

The phase selection phenomena can be nucleation-controlled, growth-controlled or both.<sup>[27]</sup> In alloy systems with numerous phases, the competition in the nucleation-controlled regime is largely determined by the relative magnitudes of  $\Delta G^*$ , *i.e.*, the energy barrier to nucleation which can be represented by the following equation<sup>[28]</sup>:

$$\Delta G^* = \frac{16\pi\gamma_{SL}^3 T_m^2 f(\theta)}{3L_f^2 \Delta T^2}. \quad [1]$$

In Eq. [1],  $\gamma_{SL}$  is the solid–liquid interface energy,  $L_f$  is the latent heat of fusion per unit volume,  $T_m$  is the melting temperature of the phase,  $f(\theta)$  is a factor related to the contact between the nucleus and a catalytic surface, and  $\Delta T$  is the undercooling below the equilibrium melting point. The above equation shows that many parameters can play a role in determining which phase nucleates more easily. There is not enough

thermodynamic data to fully compare the nucleation energy barriers of the observed borides and carbides. But based on the microstructural evolutions and possibility of sudden changes in the type of constituent phases, it seems reasonable to assume that substantial differences exist between the properties of the observed phases such as their interfacial energy or preferred level of undercooling. During solidification of a liquid metal, the non-equilibrium effects or the level of liquid metastability can be evaluated by the amount of the undercooling below the equilibrium melting point.<sup>[29]</sup> In fact, among the above-mentioned parameters, the solidification microstructure is closely related to the level of undercooling at the onset of nucleation.<sup>[18]</sup>

While the amount of undercooling can be accurately controlled and measured in some processes (*e.g.*, solidification of suspended liquid droplets<sup>[18]</sup>), the same measurement is not easy to perform during deposition on a substrate followed by continuous rapid cooling as happens in laser cladding process. However, the connection between undercooling and cooling rate can be used to predict the variations of undercooling during the laser deposition process. In general, increasing the cooling rate tends to enhance undercooling.<sup>[30]</sup> As a result, the observed microstructural evolutions in samples solidified with higher cooling rates can be correlated to their higher level of undercooling.

Both nucleation and growth of the competing phases can be influenced by the level of undercooling. There are many examples for the nucleation-controlled phase selection with increasing undercooling.<sup>[28]</sup> Similarly, growth of the phases can also be affected. If one phase grows much more rapidly than the other at higher undercoolings, that phase will finally dominate the microstructure. Sometime ease of diffusion also plays a role in selection of the final phase or microstructure, especially in alloy systems.<sup>[30]</sup> An example of this can be observed in the studied coatings in which the blocky Cr<sub>5</sub>B<sub>3</sub> particles give way to the floret-shape structures as seen in Figure 12. The dark layers in the floret-shape structures are Cr<sub>5</sub>B<sub>3</sub> which were formed during a metastable eutectic reaction.<sup>[7]</sup> The thickness of these layers is around 100 nm and they are separated by layers of Ni solid solution. The diffusion length for the alloying elements is much shorter in such morphology in comparison to bulky Cr<sub>5</sub>B<sub>3</sub>. This may explain why the floret-shape structures are dominant although the bulky Cr<sub>5</sub>B<sub>3</sub> particles were able to nucleate. EBSD data shows that when floret-shape structures overtake the blocky Cr<sub>5</sub>B<sub>3</sub> precipitates, the Cr<sub>5</sub>B<sub>3</sub> layers inside the florets keep the same crystallographic orientation as the primary Cr<sub>5</sub>B<sub>3</sub> precipitates. Figure 13 presents an example of the transition from blocky Cr<sub>5</sub>B<sub>3</sub> precipitates to floret-shape structures. The [001] IPF map of Figure 13(c) shows that there are two Cr<sub>5</sub>B<sub>3</sub> grains at the center and the layers of Cr<sub>5</sub>B<sub>3</sub> on each side follow the orientation of one of the two grains during their growth. In other words, a new nucleation process did not happen and only the transition of the original phase to a more kinetically favorable structure occurred. This is an example of growth competition and shows that if the growth kinetics of the primary phase is not fast enough,

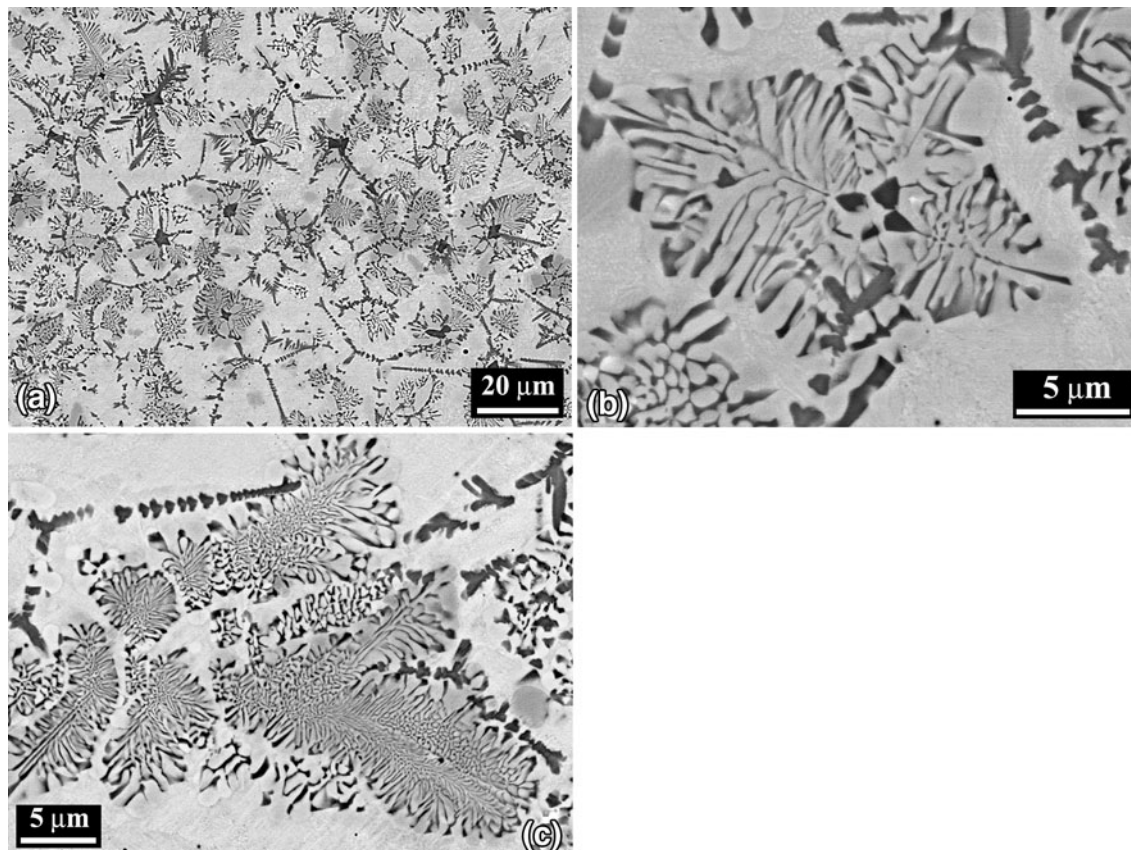


Fig. 12—(a) SEM-BSE image showing how the floret-shape phases dominate the microstructure although many started as blocky  $\text{Cr}_5\text{B}_3$ . The dendritic phase is  $\text{Cr}_7\text{C}_3$ . (b) A close-up look at how the floret-shape structure started as a blocky  $\text{Cr}_5\text{B}_3$  but later transformed. (c) Direct formation of the floret-shape structures from the melt.

it may be replaced or overtaken by another more rapid structure.<sup>[30]</sup>

Not all floret-shape structures were formed because of transition from blocky  $\text{Cr}_5\text{B}_3$  precipitates. In many cases, they were formed directly from the melt as shown in Figure 12(c). These observations suggest that the floret-shape structures had a better chance of nucleation and/or growth at higher levels of undercooling.

Figures 12 and 13 suggest that the transition in the boride formation reaction can happen during both nucleation and growth. In other words, the floret-shape phases can form either directly from the highly undercooled melt or by outgrowing the blocky  $\text{Cr}_5\text{B}_3$ . Previous research showed that when the interface attachment kinetics of the competing phases are comparable, then the competitive nucleation principles apply but if there is a significant difference of two or three orders of magnitude in the interface growth kinetics, the phase selection process will be growth-controlled. The differences in the interface attachment kinetics can be caused by several factors including the level of order in the phase (e.g., an ordered intermetallic phase vs a disordered solid solution) and the complexity of the crystal structure.<sup>[27]</sup> The layers of  $\text{Cr}_5\text{B}_3$  in the floret-shape structures have the same crystal structure, level of structural order and even crystal orientation as the blocky  $\text{Cr}_5\text{B}_3$ . As a result, their interfaces with the melt should have similar mobility. However, the growth

of their interfaces can still be influenced by the ease of diffusion as a result of their different length scales.

Most of the observed phases in this alloy system can be found in the relevant binary and ternary equilibrium diagrams.<sup>[5,21,31]</sup> While from the thermodynamics point of view all of the observed phases could form (either as stable or metastable phases), at the end the kinetic and diffusion processes determined which of the possible phases and microstructures could actually appear. If the alloy composition has the potential to follow various phase formation pathways, different phase selection phenomena can occur. Further analysis and experiments are necessary to clarify the exact mechanisms of phase selection during rapid solidification of Ni-Cr-B-Si hard-facing alloys.

### C. Effects of Boride Selection on the Eutectic Structures

The DTA graphs of Figure 3 showed that the higher cooling rates mostly influenced the formation of boride phases at higher temperatures. However, as nucleation and growth of the boride phases at the early stages of solidification determine the amount of boron remaining in the melt pool, the boride phase selection processes may have implications for the Ni-B eutectic reactions. In the microstructure of Figure 7(b), the dominant type of boride phase is  $\text{CrB}$  which contains around 17 wt pct of boron. On the other hand, the thin layers of  $\text{Cr}_5\text{B}_3$  in the



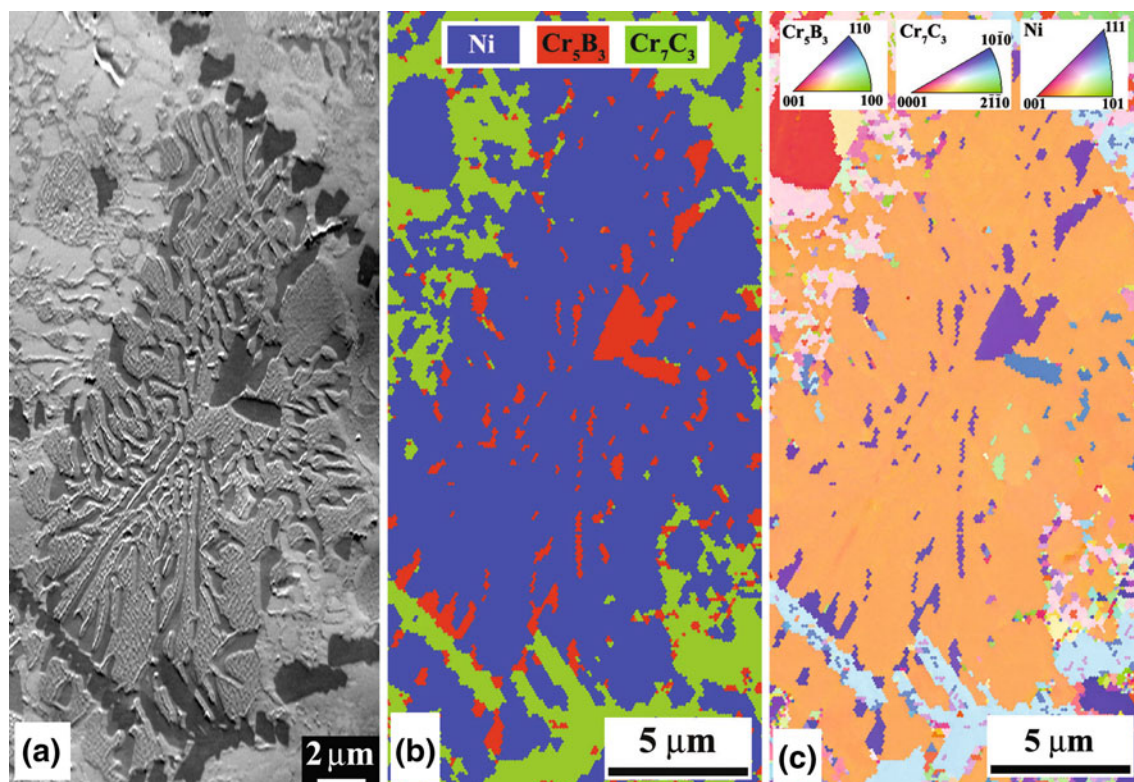


Fig. 13—(a) SEM image of a blocky  $\text{Cr}_5\text{B}_3$  surrounded by a floret-shape structure, (b) phase map, and (c) [001] IPF map of the area in (a). In (c), the way orientation of  $\text{Cr}_5\text{B}_3$  layers follows that of the blocky precipitates is noticeable. Boundary misorientation is 5 deg.

floret-shape structures of Figure 7(c) contain around 11 wt pct of B.<sup>[31]</sup> Formation of a boride phase with lower boron content will keep more boron available for the Ni-B eutectic reactions. This will increase the content of the Ni-B-Si eutectic structures and also the portion of the harder Ni-B eutectic phases.<sup>[5]</sup> So, the higher percentage of the eutectic structures in the microstructure of Figure 7(c) in comparison to that of Figure 7(b) can be attributed to the different boride formation reactions of these two microstructures. Given the high hardness of the eutectics as shown in Figure 8(b), changes in the content of eutectic phases can explain the variations in the microhardness of the deposits.

#### D. The Sequence of Phase Formation

Although a multi-component phase diagram for Ni-Cr-B-Si-C alloys does not exist in the literature, based on the finding of this study, it is possible to predict the sequence of phase formation in this alloys system. The peritectic transformation as discussed in Section III-G-2 indicates that CrB is the first phase to solidify followed by  $\text{Cr}_5\text{B}_3$ . Furthermore, nucleation of  $\text{Cr}_7\text{C}_3$  on either CrB or  $\text{Cr}_5\text{B}_3$  as presented in Figure 11 shows that this phase forms at a lower temperature and nucleates on the existing CrB or  $\text{Cr}_5\text{B}_3$  precipitates. Similarly, envelopes of Ni around the borides precipitates (Figure 7) can be regarded as a sign of their lower temperature of formation. If primary CrB or  $\text{Cr}_5\text{B}_3$  is suppressed at higher undercoolings,  $\text{Cr}_7\text{C}_3$  will be accompanied by the floret-shape structures. The Ni-B-Si eutectics are the last

phases to solidify under all conditions. They always form a continuous network and fill the spaces between the precipitates and Ni dendrites or the floret-shape structures.

As mentioned before, the two categories of microstructures did not coexist. The microstructure with the blocky borides forms at a higher temperature range in comparison to the floret-shape structures. Formation of blocky borides depletes the melt out of boron and as a result, the first category of microstructures is free from floret-shape structures. On the other hand, the floret-shape structures can form only if formation of blocky borides is inhibited by increasing the cooling rate, *i.e.*, providing the melt with more undercooling.

#### V. CONCLUSIONS

An experimental study was executed to evaluate the effects of thermal conditions on phase formation and microstructural evolution during rapid solidification of a laser-deposited Ni-Cr-B-Si-C hardfacing alloy. The following conclusions can be made:

1. Higher cooling rates facilitated the preferential nucleation and growth of the floret-shape mixtures of Ni and  $\text{Cr}_5\text{B}_3$  via a metastable reaction in comparison to precipitation of primary CrB and  $\text{Cr}_5\text{B}_3$  borides.
2. Variation in the type of the borides also influenced the nature and proportion of the Ni-B-Si eutectics

by changing the amount of the boron remaining in the melt pool.

3. CET in the Ni dendrites could be explained in terms of variations in the temperature gradient in the melt pool and the solid–liquid interface growth velocity.
4. Microstructural evidence such as peritectic transformation of CrB and nucleation of Cr<sub>7</sub>C<sub>3</sub> on Cr borides indicated that the phase formation reactions started with precipitation of primary CrB and then Cr<sub>5</sub>B<sub>3</sub> followed by Cr<sub>7</sub>C<sub>3</sub> carbides, Ni solid solution dendrites and Ni-B-Si eutectics. Alternatively, the primary borides could be substituted with the floret-shape mixtures of Ni and Cr<sub>5</sub>B<sub>3</sub> at higher cooling rates.

## ACKNOWLEDGMENTS

This research was carried out under project number MC7.06259 in the framework of the Research Program of the Materials innovation institute M2i ([www.m2i.nl](http://www.m2i.nl)). The Wall Colmonoy Ltd. (The U.K.) is acknowledged for providing Colmonoy 69 powder.

## REFERENCES

1. Q. Ming, L.C. Lim, and Z.D. Chen: *Surf. Coat. Technol.*, 1998, vol. 106, pp. 174–82.
2. J.M. Miguel, J.M. Guilemany, and S. Vizcaino: *Tribol. Int.*, 2003, vol. 36, pp. 181–87.
3. E. Fernández, M. Cadenas, R. González, C. Navas, R. Fernández, and J. de Damborenea: *Wear*, 2005, vol. 259, pp. 870–75.
4. A. Conde, F. Zubiri, and Y.J. De Damborenea: *Mater. Sci. Eng. A*, 2002, vol. 334, pp. 233–38.
5. T. Kanichi and K. Hidaka: U.S. Patent No. 4404049, 1984.
6. I. Hemmati, V. Ocelik, and J.Th.M. De Hosson: in *Contact Mechanics and Surface Treatments X*, WIT Press, Malta, 2011, pp. 287–96.
7. I. Hemmati, J.C. Rao, V. Ocelik, and J.Th.M. De Hosson: *Microsc. Microanal.*, 2013, vol. 19, pp. 1–12.
8. C.R. Das, S.K. Albert, A.K. Bhaduri, C. Sudha, and A.L.E. Terrance: *Surf. Eng.*, 2005, vol. 21, pp. 290–96.
9. T.A.M. Haemers, D.G. Rickerby, F. Lanza, F. Geiger, and E.J. Mittemeijer: *J. Mater. Sci.*, 2000, vol. 35, pp. 5691–98.
10. D. Kesavan and M. Kamaraj: *Surf. Coat. Technol.*, 2010, vol. 204, pp. 4034–43.
11. R. Kaul, P. Ganesh, S.K. Albert, A. Jaiswal, N.P. Lalla, A. Gupta, C.P. Paul, and A.K. Nath: *Surf. Eng.*, 2003, vol. 19, pp. 269–73.
12. I. Hemmati, V. Ocelik, and J.Th.M. De Hosson: *Mater. Lett.*, 2012, vol. 84, pp. 69–72.
13. E. Toyserkani: *Laser Cladding*, CRC Press, Boca Raton, FL, 2005.
14. J.D. Kim and Y. Peng: *KSME Int. J.*, 2000, vol. 14, pp. 851–60.
15. R. Kenderjewski, I. Kreja, and G. Śliwiński: *Mater. Sci. Eng. A*, 2004, vol. 379, pp. 313–20.
16. D. Wang, E. Liang, M. Chao, and B. Yuan: *Surf. Coat. Technol.*, 2008, vol. 202, pp. 1371–78.
17. G.S. Upadhyaya: *Powder Metallurgy Technology*, Cambridge International Science Publications, Cambridge, 2002.
18. J.H. Perepezko, J.L. Sebright, P.G. Höckel, and G. Wilde: *Mater. Sci. Eng. A*, 2002, vol. 326, pp. 144–53.
19. I. Hemmati, V. Ocelik, and J.Th.M. Hosson: *JOM*, 2013, vol. 65, pp. 741–48.
20. V. Ocelik, I. Furár, and J.Th.M. De Hosson: *Acta Mater.*, 2010, vol. 58, pp. 6763–72.
21. C.E. Campbell and U.R. Kattner: *CALPHAD*, 2002, vol. 26, pp. 477–90.
22. D.H. StJohn and L.M. Hogan: *Acta Metall. Mater.*, 1977, vol. 25, pp. 77–81.
23. D.H. StJohn: *Acta Metall. Mater.*, 1990, vol. 38, pp. 631–36.
24. N.A. Berjeza, S.P. Velikevitch, V.I. Mazhukin, I. Smurov, and G. Flamant: *Appl. Surf. Sci.*, 1995, vol. 86, pp. 303–09.
25. W. Kurz and R. Trivedi: *Mater. Sci. Eng. A*, 1994, vols. 179–180, pp. 46–51.
26. S. Kou: *Welding Metallurgy*, Wiley-Interscience, Hoboken, NJ, 2003.
27. M. Li, S. Ozawa, and K. Kuribayashi: *Philos. Mag. Lett.*, 2004, vol. 84, pp. 483–93.
28. J. Perepezko, L. Brewer, and R. Schaefer: *Mater. Sci. Eng.*, 1985, vol. 70, pp. 9–22.
29. D.M. Herlach: *Mater. Sci. Eng. A*, 1997, vols. 226–228, pp. 348–56.
30. J.H. Perepezko: *Prog. Mater. Sci.*, 2004, vol. 49, pp. 263–84.
31. H. Baker, ed.: *ASM Handbook-Alloy Phase Diagrams*, 10th ed., ASM International, Materials Park, OH, 1992.
32. F. Cverna, ed.: *ASM Ready Reference: Thermal Properties of Metals*, ASM International, Materials Park, OH, 2002.